The Astrophysical Journal Letters, 954:L52 (11pp), 2023 September 10 https://doi.org/10.3847/2041-8213/acebf0

Water Absorption in the Transmission Spectrum of the Water World Candidate GJ 9827 d

Pierre-Alexis Roy[1], Björn Benneke[1], Caroline Piaulet[1], Michael A. Gully-Santiago[2], Ian J. M. Crossfield[3], Caroline V. Morley[2], Laura Kreidberg[4], Thomas Mikal-Evans[4], Jonathan Brande[3], Simon Delisle[1], Thomas P. Greene[5], Kevin K. Hardegree-Ullman[6], Travis Barman[7], Jessie L. Christiansen[8], Diana Dragomir[9], Jonathan J. Fortney[10], Andrew W. Howard[11], Molly R. Kosiarek[10], and Joshua D. Lothringer[12]
[1] Department of Physics and Trottier Institute for Research on Exoplanets, Université de Montréal, Montreal, QC, Canada; pierre-alexis.roy@umontreal.ca
[2] Department of Astronomy, University of Texas at Austin, Austin, TX 78712, USA
[3] Department of Physics and Astronomy, University of Kansas, 1082 Malott, 1251 Wescoe Hall Drive, Lawrence, KS 66045, USA
[4] Max Planck Institute for Astronomy, Königstuhl 17, D-69117 Heidelberg, Germany
[5] Space Science and Astrobiology Division, NASA Ames Research Center, MS 245-6, Moffett Field, CA 94035, USA
[6] Steward Observatory, The University of Arizona, Tucson, AZ 85721, USA
[7] Lunar and Planetary Laboratory, The University of Arizona, 1640 East University Boulevard, Tucson, AZ 85721, USA
[8] Caltech/IPAC, M/S 100-22, 1200 East California Boulevard, Pasadena, CA 91125, USA
[9] Department of Physics and Astronomy, University of New Mexico, 1919 Lomas Boulevard NE, Albuquerque, NM 87131, USA
[10] Department of Astronomy & Astrophysics, University of California, Santa Cruz, CA 95064, USA
[11] Department of Astronomy, California Institute of Technology, Pasadena, CA 91125, USA
[12] Department of Physics, Utah Valley University, 800 W. University Parkway, Orem, UT 84058, USA
Received 2023 May 29; revised 2023 July 19; accepted 2023 July 29; published 2023 September 12

Abstract

Recent work on the characterization of small exoplanets has allowed us to accumulate growing evidence that sub-Neptunes with radii greater than $\sim$2.5 $R_\oplus$ often host H_2/He-dominated atmospheres both from measurements of their low bulk densities and from direct detections of their low mean molecular mass atmospheres. However, the smaller sub-Neptunes in the 1.5–2.2 $R_\oplus$ size regime are much less understood and often have bulk densities that can be explained either by the H_2/He-rich scenario or by a volatile-dominated composition known as the "water world" scenario. Here we report the detection of water vapor in the transmission spectrum of the 1.96 ± 0.08 $R_\oplus$ sub-Neptune GJ 9827 d obtained with the Hubble Space Telescope (HST). We observe 11 HST Wide Field Camera 3 transits of GJ 9827 d and find an absorption feature at 1.4 μm in its transit spectrum, which is best explained (at 3.39σ) by the presence of water in GJ 9827 d's atmosphere. We further show that this feature cannot be caused by unocculted starspots during the transits by combining an analysis of the K2 photometry and transit light source effect retrievals. We reveal that the water absorption feature can be similarly well explained by a small amount of water vapor in a cloudy H_2/He atmosphere or a water vapor envelope on GJ 9827 d. Given that recent studies have inferred an important mass-loss rate ($>0.5\,M_\oplus\,\mathrm{Gyr}^{-1}$) for GJ 9827 d, making it unlikely to retain a H-dominated envelope, our findings highlight GJ 9827 d as a promising water world candidate that could host a volatile-dominated atmosphere. This water detection also makes GJ 9827 d the smallest exoplanet with an atmospheric molecular detection to date.

Unified Astronomy Thesaurus concepts: Exoplanet atmospheres (487); Mini Neptunes (1063); Water vapor (1791); Exoplanet atmospheric composition (2021)

1. Introduction

While many questions remain regarding the nature of sub-Neptune exoplanets, the last decade of transmission spectroscopy with the Hubble Space Telescope (HST) has shown that the larger sub-Neptunes are often best described by H_2/He-dominated atmospheres (e.g., Benneke et al. 2019a, 2019b; Mikal-Evans et al. 2020; Kreidberg et al. 2022). However, this picture is much less clear when considering sub-Neptunes that are in the smaller 1.5–2.2 $R_\oplus$ size regime, near the radius valley (Fulton et al. 2017; Fulton & Petigura 2018; Van-Eylen et al. 2018; Hardegree-Ullman et al. 2020). These planets have bulk densities that can be explained by either the H_2/He-rich sub-Neptune scenario or a volatile-dominated composition, where water (or another molecule of similar mean molecular weight) supplants H_2 and He as the most abundant atmospheric species (Rogers & Seager 2010; Luque & Pallé 2022; Rogers et al. 2023). This type of exoplanet has been long theorized and is referred to as a "water world" (Adams et al. 2008; Acuña et al. 2022).

These smaller sub-Neptunes, which are often inconsistent with extended H-dominated atmospheres with large scale heights (Aguichine et al. 2021; Piaulet et al. 2023), are also found in a smaller mass regime than the larger sub-Neptunes, making these close-in planets much more exposed to mass-loss processes (Owen 2019) and thus more likely to have lost their H_2 and He envelopes over their lifetime. A recent study found a first line of evidence for the existence of such volatile-rich water worlds in the super-Earth Kepler-138 d by combining a thorough interior analysis of the planet with mass-loss estimates, effectively showing that this super-Earth cannot be purely rocky but also cannot retain a hydrogen layer (Piaulet et al. 2023). However, the direct spectroscopic confirmation of a volatile-rich high mean molecular weight atmosphere on a

water world candidate still eludes us, and such a result would provide a new line of evidence for the water worlds.

The discovery of the transiting sub-Neptune GJ 9827 d (Niraula et al. 2017; Rodriguez et al. 2018) represents a rich opportunity to characterize the atmosphere of a warm sub-Neptune via transmission spectroscopy and to deepen our understanding of this potential water world (Aguichine et al. 2021). Rapidly orbiting (6.2 days) a low-mass K6V star with a size of $1.96 \pm 0.08\,R_{\oplus}$, a mass of $3.4 \pm 0.6\,M_{\oplus}$ (Kosiarek et al. 2021), and a zero-albedo equilibrium temperature of 680 ± 25 K (Rodriguez et al. 2018), GJ 9827 d allows us to obtain a high signal-to-noise ratio (S/N) in transmission spectroscopy and add a precious new target to the sample of sub-Neptunes with transit spectra. While JWST now allows one to observe the eclipses and phase curves of small exoplanets deeper in the infrared (e.g., Kempton et al. 2023), transit spectroscopy remains the best method to obtain in-depth looks into the atmospheres of sub-Neptunes and potential water worlds with HST, as they are rarely hot enough to provide a high S/N in the near-infrared (hot Neptune desert; Owen & Lai 2018).

While the average density of GJ 9827 d has now been constrained ($>3\sigma$) by numerous radial velocity studies of the system (Prieto-Arranz et al. 2018; Rice et al. 2019; Kosiarek et al. 2021), there still remains ambiguity regarding its bulk composition, as its density could be explained by a range of compositions from an extended H_2/He layer to a water world with a ~20% water mass fraction (Aguichine et al. 2021). However, the high irradiation of the planet, the old age of the system (Kosiarek et al. 2021), and the nondetections of He I and Hα absorption from the ground (Kasper et al. 2020; Carleo et al. 2021; Krishnamurthy et al. 2023) make it unlikely that GJ 9827 d would have retained a primordial H-dominated envelope to date.

In this work, we present the most precise look yet at GJ 9827 d via transmission spectroscopy with the HST Wide Field Camera 3 (WFC3) and reveal a water absorption feature in its transmission spectrum. In Section 2, we present the observations obtained for this study, and we describe the data analysis in Section 3. Section 4 presents our atmospheric analysis of the HST transit spectrum, and the related results are presented in Section 5. We end by discussing our findings and presenting our conclusions in Section 6.

2. Observations and Data Reduction

The sub-Neptune GJ 9827 d was observed transiting its host star 11 times between 2017 December and 2020 December with the WFC3 on board the HST as part of the mini-Neptune atmosphere diversity survey (GO 15333; PI: Crossfield). The G141 grism was used in order to obtain the transmission spectrum of the sub-Neptune over the 1.1–1.7 μm range.

Each of the 11 HST/WFC3 transit observations consisted of ~3 hr of observing time spanning three telescope orbits with ~1 hr gaps between them. Each transit observation is thus composed of one orbit before, during, and after transit. The transit time series were obtained with the G141 grism using the spatial scan mode. In order to optimize the duty cycle of our observation, we use both the forward and backward detector scans. We discard one of the transits from our analysis (2019 November 1), since a pointing maneuver cut orbit 1 short before the ramp was stabilized, effectively carrying an unusually strong ramp to orbit 2 and polluting the in-transit observations.

We reduce the observations following standard procedures for HST/WFC3 observations (details in Benneke et al. 2019a, 2019b). In order to minimize the background contribution, we subtract consecutive reads up the ramp and then add together the background-subtracted frames. We then construct flat-fielded images from the flat-field data product provided by STScI. We use a normalized row-added flux template in order to remove and replace outlier pixels in our frames. We follow Benneke et al. (2019a) in order to correct for the slight slanted shape of the trace on the detector, which is introduced by the spatial scan mode, using a trapezoidal shape integration scheme for the wavelength bins, which we choose to be 30 nm wide. Our flux integration does not perform presmoothing and does account for partial pixels along the trapezoidal bin boundaries. Finally, in order to account for the small drift of the star across the detector during the observations, we account for a small position shift that is measured in each frame.

3. Data Analysis

We perform the light-curve fitting of our 10 transits of GJ 9827 d individually using the ExoTEP framework (Benneke et al. 2017, 2019a, 2019b). We use ExoTEP to jointly fit the transit model with a systematics model and a photometric noise parameter in a Markov Chain Monte Carlo (MCMC) scheme (Foreman-Mackey et al. 2013). We decide to fit the transits individually, since they display variability in the transit timings (see Figures 1 and 2 and Section 6.1).

Each visit in our data set consists of three HST orbits that do not cover the full transit duration of GJ 9827 d (Figure 1). The in-transit observations only occur during the second orbit of each visit, observing either the ingress, the middle of the transit, or the egress (Figure 1). For that reason, we cannot obtain reliable constraints on the orbital parameters out of the partial transit observations and decide to use a fixed orbital solution during the fits ($b = 0.91$, $a/R_{\star} = 19.88$).

Since the visits do not include a burn-in orbit, we cannot follow the standard procedure to discard the first orbit, which displays a stronger ramp in time as the detector is still settling (e.g., Kreidberg et al. 2014). We rather choose to keep the two to four last points of orbit 1 in each visit (Figure 1), as the strong ramp has stabilized by then, and it provides essential baseline information, especially for visits that only have mid-transit or egress data in orbit 2 (Figure 1). For all orbits, we discard the first forward and backward scans.

Because GJ 9827 is a close-in, near-resonant system, some of the visits in our data set also include transits of GJ 9827 b. Given the partial coverage of our visits, we simply remove the points where GJ 9827 b is expected to transit, which affects visits 5 and 10. Visits 6 and 7 also include a transit of planet b, but it happens in the first orbit which is already mostly discarded. Finally, we remove the last five points of visit 3, since they are clear outliers.

3.1. White Light-curve Fit

We fit for systematics trends in the normalized transit light curves simultaneously with the transit model using an analytical model that allows for a linear slope throughout the visit duration and an exponential ramp in each orbit. Following previous work (e.g., Kreidberg et al. 2014; Benneke et al. 2019b),

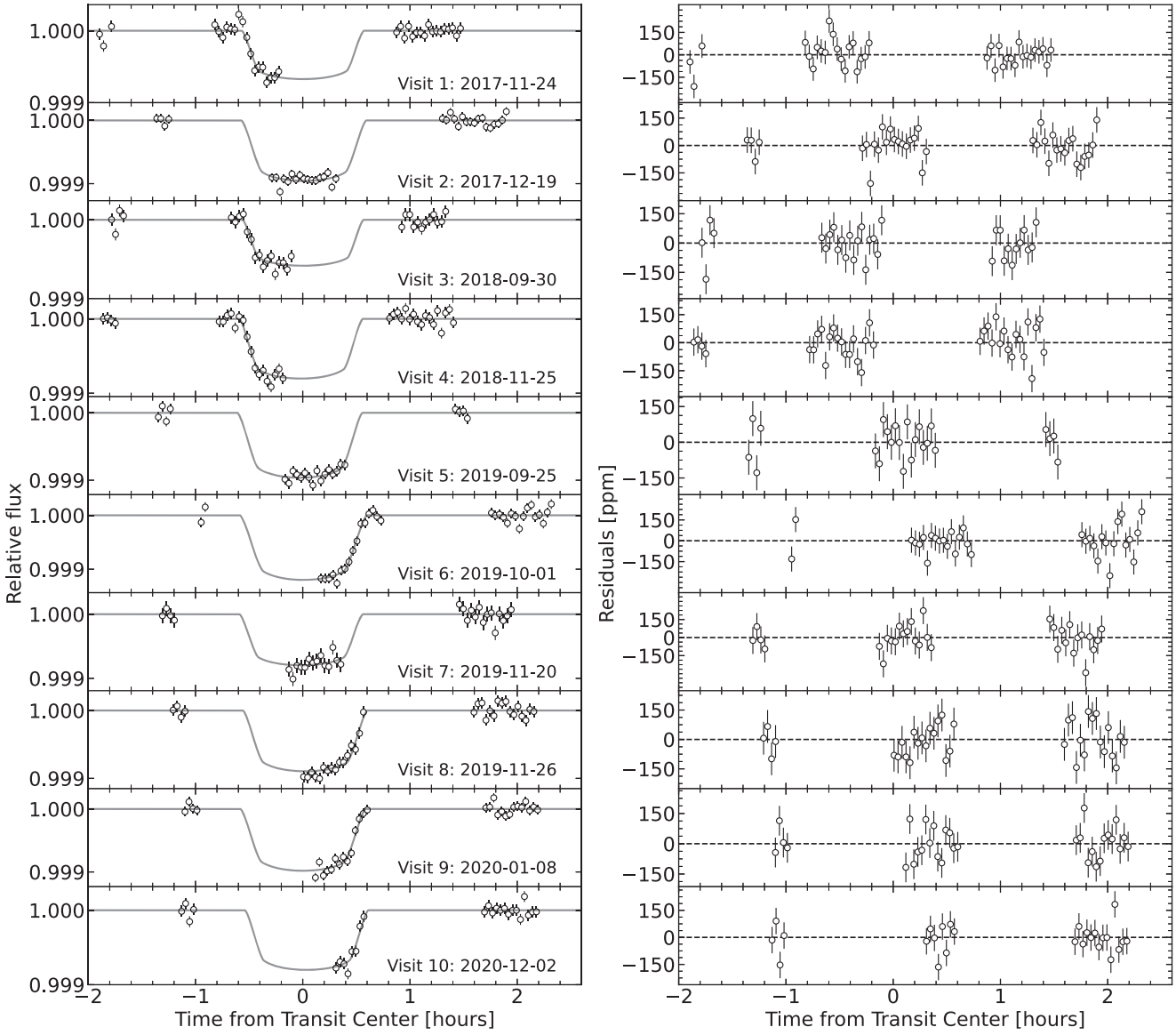

Figure 1. All 10 HST/WFC3 broadband light-curve fits of the transits of GJ 9827 d. Left: systematics-corrected and normalized broadband light curves for the 10 transits of GJ 9827 d (data points). Each visit is centered around the fitted transit time for that visit. The best-fitting transit model is also shown as the gray line. Right: residuals of the broadband light-curve fits shown on the left.

we use the following parameterization to account for these systematics:

$$S_{\rm model}(t) = (c\,S(t) + v\,t_v) \times (1 - e^{(-a\,t_{\rm orb} - b - d)}). \quad (1)$$

Here c is the normalization constant, v is the linear slope throughout the visit, a and b are the rate and amplitude of the exponential ramp in each orbit, d is an offset only for first orbit reads, and $S(t)$ is a function that is equal to 1 for forward scans and s for backward scans, allowing one to correct for the offset between forward and backward scans. Finally, t_v is the time since the start of the visit, while $t_{\rm orb}$ is the time since the start of the orbit.

We produce our transit light-curve models using the Batman package (Kreidberg 2015). Since we are not trying to fit the orbital solution, the only two astrophysical parameters that we are fitting in the transit light curve are the transit depth and mid-transit time (Figure 2). For the limb darkening, we use the Exotic-LD package (Grant & Wakeford 2022) to compute the coefficients using 1D stellar models (Kurucz 1993) and the quadratic limb-darkening law. The impact parameter and semimajor axis are set to the values in Niraula et al. (2017). We obtain the posterior distribution on our parameters by running an MCMC analysis individually for each of the 10 visits. We use four walkers per parameter, and all priors are uniform. The 10 white light-curve fits are shown in Figure 1.

3.2. Spectroscopic Light-curve Fit

We use the white light-curve fit results in terms of the systematics model to precorrect the light curves in each spectral bin (the divide-white method; Stevenson et al. 2014). Thus, we

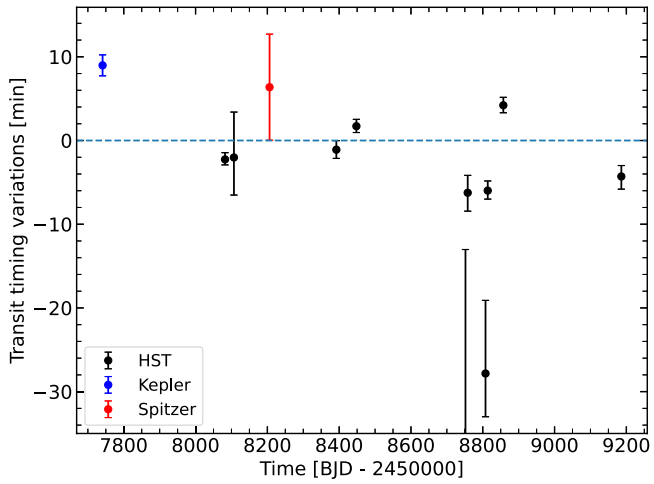

Figure 2. Observed mid-transit time (black points) for each of the 10 transits compared to a fitted linear ephemeris to all transit timings presented (except the two timings with large uncertainties; $T_{0,BJD} = 2459185.987 \pm 0.002$, $P = 6.20186 \pm 0.00002$ d). The ephemeris derived from the K2 campaign is shown (blue; Niraula et al. 2017) along with the Spitzer transit for this planet (red; Kosiarek et al. 2021). Our 10 HST/WFC3 transits suggest that there are statistically significant TTVs in the orbit of GJ 9827 d of the order of 5–10 minutes.

Table 1
HST/WFC3 Near-infrared Combined Spectrum of GJ 9827 d

Instrument	Wavelength (μm)	Depth (ppm)	$\pm1\sigma$ (ppm)
HST/WFC3	1.10–1.13	941.3	59.7
	1.13–1.16	1003.3	28.3
	1.16–1.19	939.6	24.5
	1.19–1.22	945.5	23.4
	1.22–1.25	987.7	22.4
	1.25–1.28	965.7	18.8
	1.28–1.31	921.0	22.3
	1.31–1.34	998.7	20.3
	1.34–1.37	1018.9	22.1
	1.37–1.40	986.8	21.9
	1.40–1.43	1015.4	21.2
	1.43–1.46	960.4	22.1
	1.46–1.49	982.5	23.0
	1.49–1.52	992.2	22.5
	1.52–1.55	953.8	21.3
	1.55–1.58	935.3	22.8
	1.58–1.61	919.3	23.5
	1.61–1.64	944.0	19.1
	1.64–1.67	941.2	21.9

divide the spectroscopic light curves by the white light-curve best-fitting systematics model before starting the fitting. We produce our spectroscopic transit light-curve models similarly as in the white light-curve case, but we now keep the mid-transit time fixed to the best-fitting value found by the white light-curve fit. The limb darkening is again modeled with Exotic-LD, and this time, our systematics model is a three-parameter linear slope with trace position (measured during the data reduction; see Section 2). We thus obtain 10 transmission spectra, one from each visit, by running an MCMC analysis on each. We again use four walkers per parameter and uniform priors on all parameters.

3.3. Combining All Visits Together

We compute a weighted average of our 10 individual transmission spectra to obtain our final transmission spectrum of GJ 9827 d. In order to verify the robustness of our spectrum and ensure that it is not affected by that variability in the observations, we compare the relative transit depth in each channel for each visit (Figure 3). From each spectrum, we subtract the weighted average (across wavelengths) of said spectrum, essentially making it a relative transit spectrum centered around zero. We then subtract the relative combined spectrum of all visits (also centered around zero) from each individual spectrum to effectively center each spectroscopic transit depth around zero. We then inspect this relative transit depth for each spectroscopic bin and visit in order to ensure that the points in our final transmission spectrum are not affected by outliers (Figure 3). We find that for each spectroscopic channel, all visits mostly agree with the weighted average within the error bars, and points that are inconsistent have larger error bars, which makes them much less important in the weighted average, since the weight of each point is inversely proportional to the uncertainty squared (Figure 3). The final average transmission spectrum is presented in Table 1 and Figure 4. We decide to discard the last spectroscopic channel (1.67–1.70 μm) because it is systematically lower than the rest of the spectrum and near the edge of the trace on the detector where the data are less reliable.

4. Atmospheric Modeling

We perform atmosphere retrievals on our GJ 9827 d transmission spectrum using the SCARLET framework (Benneke & Seager 2012, 2013; Knutson et al. 2014; Kreidberg et al. 2014; Benneke 2015; Benneke et al. 2019a, 2019b; Pelletier et al. 2021; Roy et al. 2022). SCARLET parameterizes the molecular abundances, cloud deck pressure, and temperature to fit our spectrum. SCARLET uses a Bayesian nested sampling analysis (with single ellipsoid sampling; Skilling 2004, 2006) to obtain the posterior probability distribution of our parameter space and the Bayesian evidence of our models.

For each set of parameters, SCARLET produces a forward atmosphere model in hydrostatic equilibrium (Benneke 2015), computes the opacity associated with each molecule throughout the 40 vertical (pressure) layers of the model, computes the transmission spectrum for that model, and performs the likelihood evaluation. The model transmission spectra produced at each step have a resolution of 16,000 and are then convolved to the wavelength bins of the observed spectrum. The molecules considered in our retrieval are H_2O, CH_4, CO_2, CO, and N_2, as well as H_2 and He, which are not parameterized and rather fill up the atmosphere (Benneke & Seager 2013).

We assume well-mixed vertical chemical profiles, where the abundances of molecules do not vary throughout the atmosphere. We choose a log-uniform prior on the abundance of each molecule ranging from 10^{-10} to 1 in volume mixing ratio. We assume a constant temperature structure throughout the atmosphere and use a Gaussian prior centered on the planet's equilibrium temperature (680 ± 100 K; Rodriguez et al. 2018) on that parameter. The parameterization also includes a cloud deck top pressure, which blocks all light rays going through that pressure level. We again use a log-uniform prior on that parameter from 10^{-4} to 10^{5} mbar. Thus, our atmosphere

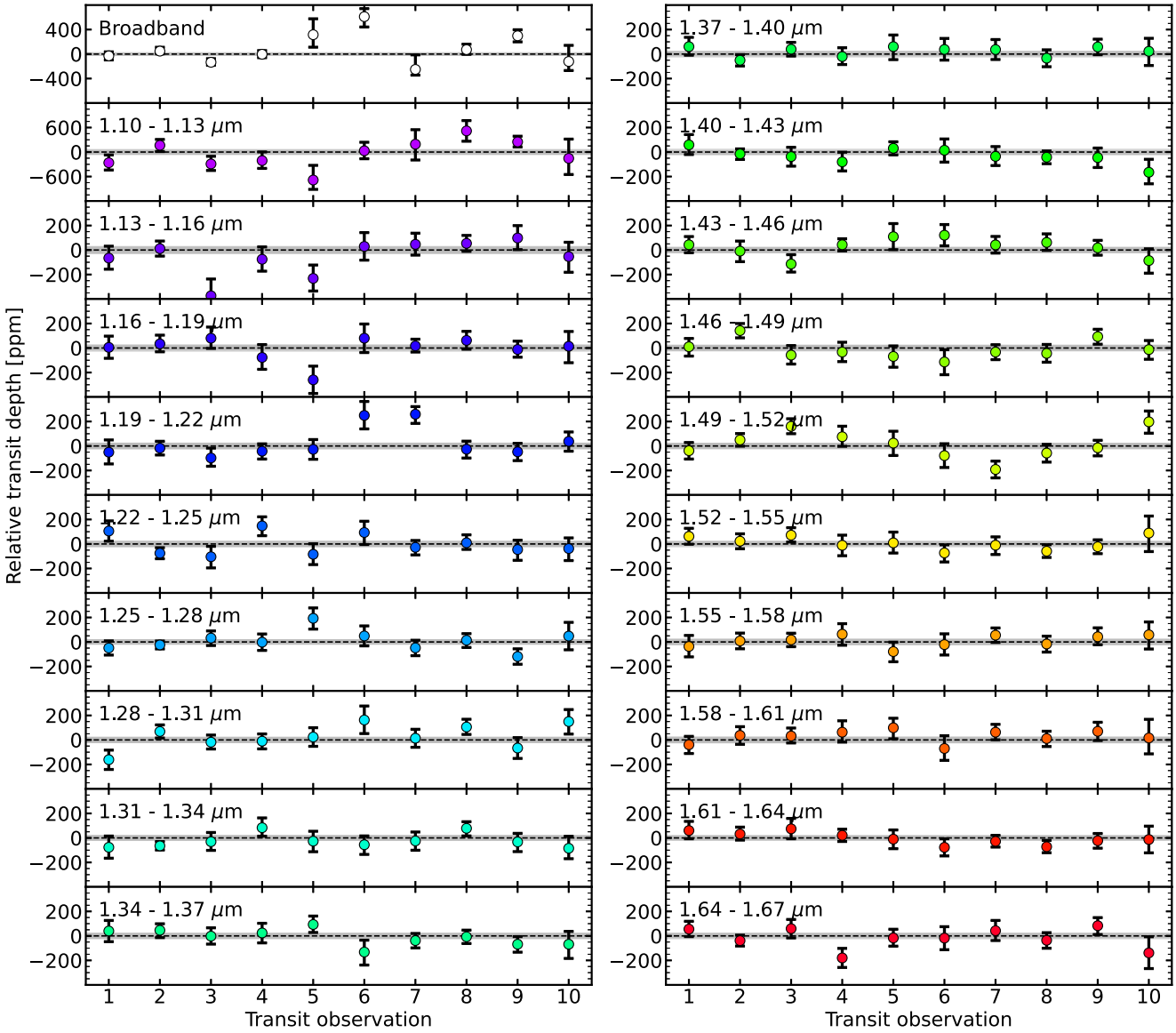

Figure 3. Individual relative transit depths compared to the relative final transmission spectrum. For each of the 10 transmission spectra, we obtain the relative transit spectrum by subtracting the average across wavelengths. We then subtract the relative final transmission spectrum from the individual relative spectra and display these transit depths for all visits in each channel. The relative transit depths are consistent across the 10 visits with the final relative spectrum. Points that are significantly away from zero (dotted lines) have larger error bars, which makes them less important in the weighted average, and thus do not bias our transmission spectrum. The uncertainty on the combined spectrum is also displayed as the gray region. In the top left panel, the broadband transit depths are shown, centered on the average across the 10 visits, highlighting the variability in the observed broadband transit depths from the different visits.

Table 2
Bayesian Model Comparison Results from Our SCARLET Atmosphere Retrievals in the Free Chemistry Setting

Retrieval Model	Evidence $\ln(Z_i)$	Bayes Factor $B = Z_{\rm ref}/Z_i$	N_σ
All molecules + clouds	−90.68	Ref.	Ref.
H_2O removed	−94.96	72.52	3.39
CH_4 removed	−90.24	0.65	0.90
CO_2 removed	−90.45	0.79	0.90
CO removed	−90.60	0.92	0.90
N_2 removed	−90.73	1.06	1.14
Clouds removed	−90.78	1.10	1.23
H_2O, CH_4 removed	−94.88	66.92	3.36
Flat spectrum	−97.11	620.76	4.01

retrieval includes seven free parameters in total (or less when molecules are removed; see Table 2).

5. Results

The observed transit spectrum of GJ 9827 d displays a water absorption feature at 1.4 μm (Figure 4). Qualitatively, the transit depths in the spectrum are deeper in the 1.4 μm water band followed by a downward slope that follows the wing of the water absorption feature. Quantitatively, a Bayesian model comparison analysis of our well-mixed retrievals (Benneke & Seager 2013) prefers models that include the presence and absorption of water with a significance of 3.39σ (Bayes factor = 72.52; Table 2) compared to models that do not include water.

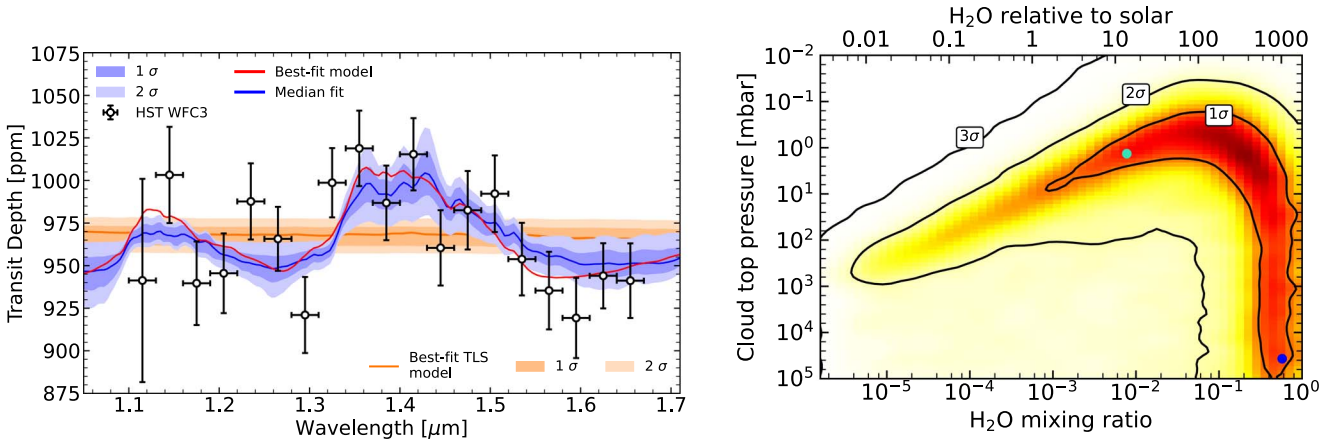

Figure 4. Water detection in the transmission spectrum of GJ 9827 d. Left: transmission spectrum of GJ 9827 d (black points) shown with our model transmission spectrum constraints from the nested sampling atmosphere retrieval (blue) and the photometry-informed TLS retrieval (orange). The dark blue and light blue shaded regions show the 1σ and 2σ Bayesian credible intervals from the atmosphere retrieval, respectively. The atmospheric median transmission model is shown in blue, and the best-fitting model is shown in red. The best-fitting TLS model is shown in orange along with the 1σ and 2σ Bayesian credible intervals in light orange. Right: joint constraints on the cloud-top pressure vs. the water mixing ratio derived from our SCARLET well-mixed retrieval. The colored shading describes the normalized probability density as a function of the water mixing ratio (assuming uniform vertical profiles) of the atmosphere and cloud-top pressure. The black contours highlight the 1σ, 2σ, and 3σ Bayesian credible regions. The water abundance relative to a solar composition atmosphere is shown on the top axis. The posterior probability distribution allows for multiple atmospheric scenarios ranging from H_2/He envelopes with small amounts of water to water-dominated envelopes. The blue points identify two representative samples of these two scenarios, which are displayed in Figure 6.

5.1. Metallicity–Cloud Degeneracy

Our free chemistry retrievals show that the data can be explained by both a water-rich atmosphere, where water is the most abundant molecule, and a H_2/He-dominated atmosphere that still contains a small amount of water (Figure 4). At 1σ, models with a water mixing ratio between 0.02% and 80% are preferred by the spectrum. When compared to the amount of water in a solar metallicity envelope, we see that this interval in abundance ranges from $1\times$ solar metallicity models that are dominated by H_2 and He gas to $1000\times$ solar metallicity models where water is now the principal species (Figure 4).

In the cases where water is present in small amounts, a cloud deck is needed to explain the observed transit spectrum (Figures 4 and 5). This is due to the fact that the observed spectrum does not display the large amplitude expected from cloud-free models (Figure 6). This need for clouds in low mean molecular weight atmospheres is also seen in the marginalized probability distributions of the other molecules (Figure 5), since their spectral features are inconsistent with the observed spectrum and thus must be muted by clouds in order to yield high-likelihood models. In cases where the water is more abundant and becomes the principal molecule, the spectra naturally display muted features because of the high density of the atmospheres and lower atmospheric scale height, thus removing the need for high clouds. In this water-rich scenario, the constraint on the cloud-top pressure disappears, explaining the observed posterior distribution (all deep cloud decks become equally consistent; Figure 4).

5.2. Upper Limits on Other Molecules

While methane is known to display a similar 1.4 μm absorption feature as water (Bézard et al. 2022), it remains disfavored in our free chemistry retrieval analysis. The spectral signatures of methane include a feature not only around 1.4 μm but also at 1.2 and 1.7 μm, as shown by SCARLET forward atmosphere models for a pure methane envelope and a solar composition atmosphere (Figure 6). However, the observed transmission spectrum of GJ 9827 d does not display these absorption features at 1.2 and 1.7 μm (Figure 6) and is in better agreement with the water models that display a smaller feature at 1.2 μm, no absorption at 1.7 μm, and a broader feature at 1.4 μm. In order to obtain chemically consistent models that agree with the observed transit spectrum, the carbon-to-oxygen (C/O) ratio must be decreased in order to favor O-bearing molecules (here, water), and a cloud deck must be included to mute the spectral amplitude of the water absorption features. Such models (e.g., C/O = 0.1, metallicity = $100\times$ solar, and pCloud = 1 mbar) yield qualitatively and quantitatively similar transmission spectra to those favored by our free chemistry retrieval (Figures 4 and 6).

No other molecule besides water is statistically detected by our retrievals (Table 2, Figure 5). However, we can derive upper limits on their abundances based on our results from the free chemistry retrievals, either from the nondetection of specific spectral features (e.g., CH_4) or because too much of any one species increases the mean molecular weight of the atmosphere, eventually yielding a flat spectrum (e.g., N_2). Thus, our retrievals allow us to constrain the upper limits on the mixing ratios of CH_4, CO_2, CO, and N_2 to 3.04%, 19.4%, 52.5%, and 60.4% at 3σ significance.

5.3. Significance of a Featureless Spectrum

In order to evaluate how our spectrum deviates from a featureless spectrum, we compute the deviation from the best-fitting straight line using χ^2 statistics. Using the binned version (bottom panel of Figure 6), we obtain that the transmission spectrum of GJ 9827 d deviates from a straight line at 3.24σ. In order to assess how our water detection compares to a featureless flat spectrum within the Bayesian paradigm, we compute the Bayesian evidence of a one-parameter flat line model $\mathcal{Z}_{\rm flat}$. Given the simplicity of this one-parameter model, we do not need to use SCARLET nested sampling to obtain that value. Rather, we numerically estimate it via the following

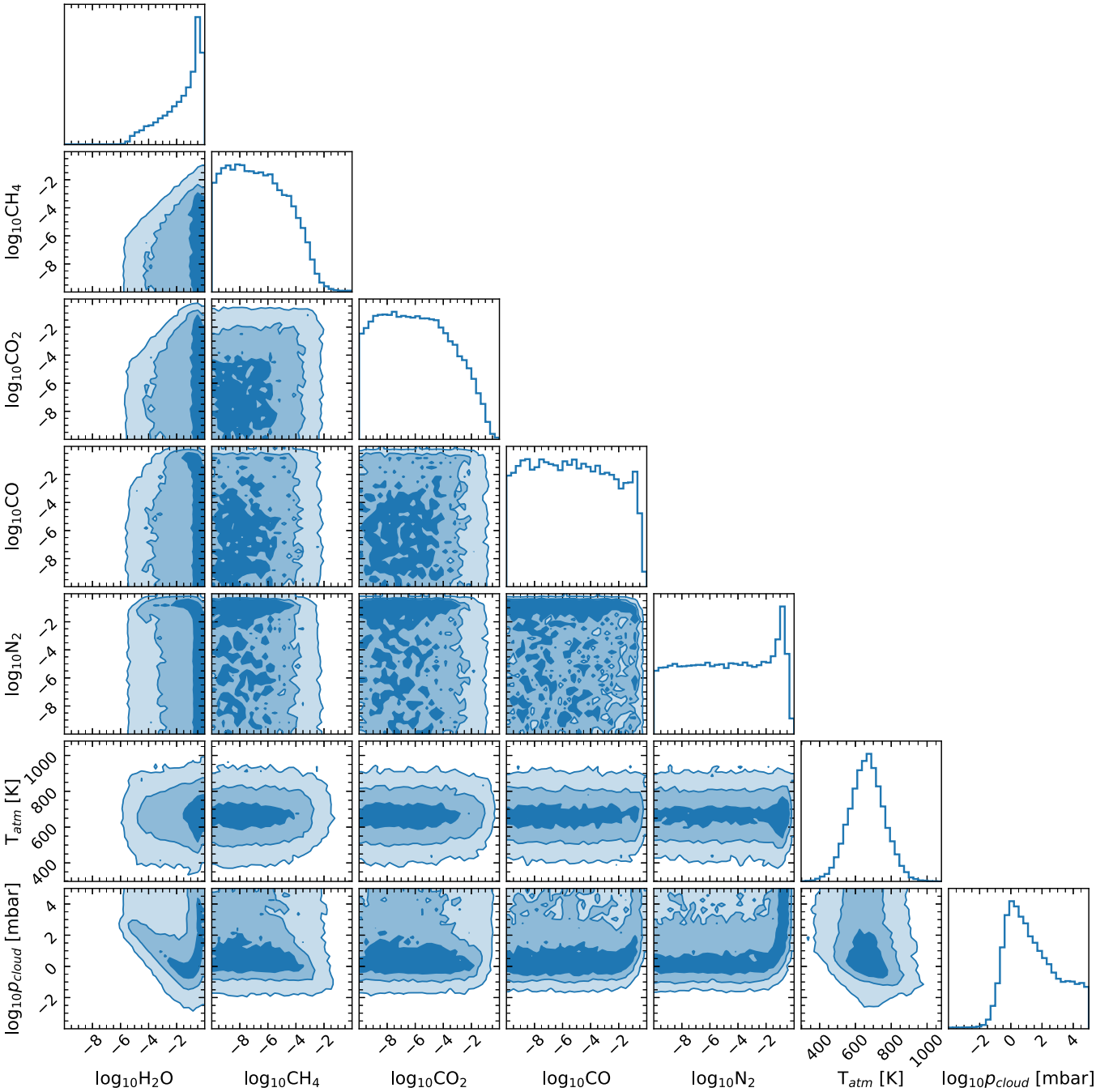

Figure 5. Posterior probability distributions of the free parameters used in the SCARLET free chemistry retrieval. The diagonal panels show the marginalized probability distributions of all individual parameters, whereas the off-diagonal panels show the marginalized probability distributions for each pair of parameters as colored shading. The 1σ, 2σ, and 3σ contours are shown in the 2D posteriors. Water is the only molecule detected in our retrieval analysis.

analytical solution:

$$\mathcal{Z}_{\rm flat} = \left(\frac{1}{\sqrt{2\pi}}\right)^N \times \left(\prod_{i=1}^{N} \frac{1}{\sigma_i}\right) \times \left(\frac{1}{\theta_2 - \theta_1}\right) \times \int_{\theta_1}^{\theta_2} \exp\left(-\sum_{i=1}^{N} \frac{(D_i - \theta)^2}{2\sigma_i^2}\right) d\theta, \quad (2)$$

where N is the number of points in the spectrum; σ_i is the uncertainty of the ith point of the spectrum, denoted D_i; and θ_1 and θ_2 are the limits of our uniform prior on the transit depth parameter θ. This allows us to show that our atmosphere model is preferred to the flat spectrum model at 4.01σ (Bayes factor = 620.76; Table 2).

5.4. Ruling Out Stellar Contamination

The transit light source effect (TLS; Rackham et al. 2018) can mimic water features at the 20 ppm level or more for modestly spotted stars under certain observational configurations and could thus create the feature observed in our transmission spectrum. The best constraint available for the starspot coverage and contrast for GJ 9827 comes from the K2

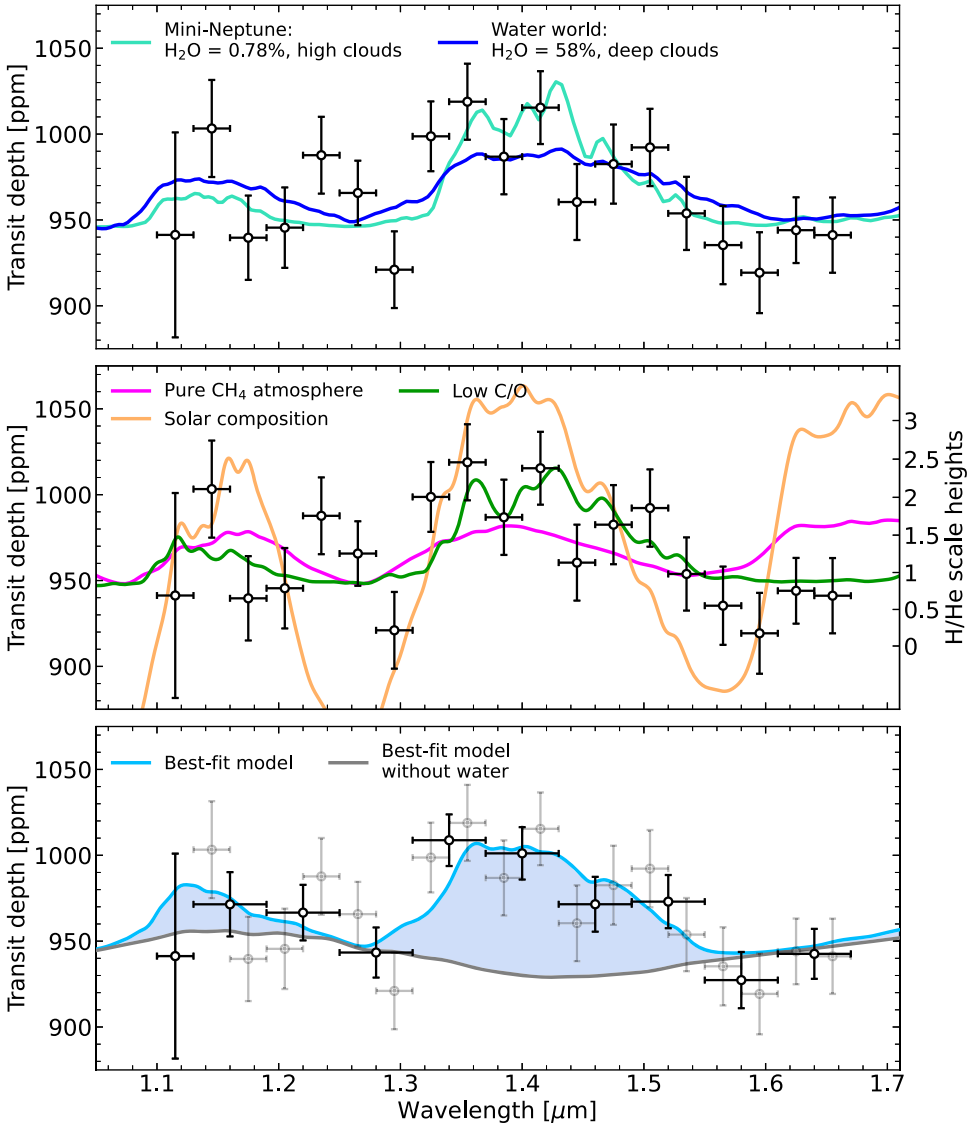

Figure 6. The HST/WFC3 transmission spectrum of GJ 9827 d (data points) along with SCARLET forward atmosphere models (colored lines). In the top panel, two samples from our well-mixed retrieval analysis (Figure 4) are shown, representing the mini-Neptune scenario with a cloudy H_2/He atmosphere composed of ∼1% water (light blue) and a water world scenario with a water-rich atmosphere (dark blue). In the middle panel, a secondary atmosphere model for a pure methane envelope is also shown (magenta) in order to highlight the methane absorption features. Chemically consistent models (still assuming a uniform temperature profile) are shown for a cloud-free solar composition case (solar metallicity, solar C/O; orange) and a cloudy case with C/O = 0.1 and a 100× solar metallicity (green). The observed spectrum is inconsistent with cloud-free low-metallicity scenarios and prefers water absorption features to methane absorption features, mainly around 1.2 and 1.65 μm. The strength of the features in the spectrum is also displayed in units of H/He scale heights (right axis). In the bottom panel, the best-fit model from the retrieval analysis is shown (light blue) along with the transmission spectrum of the same model once the water opacity is turned off (gray). The contribution of water opacity to the spectral signatures is highlighted in blue. We also present a binned version of the transmission spectrum, where the points are binned together by pair with the exception of the blue-most channel.

Campaign 12 (C12) light curve, with a "self-flat-fielding"-derived (Vanderburg & Johnson 2014) peak-to-valley amplitude of 0.45%, slightly lower than the typical 0.7% for K6 spectral types (Rackham et al. 2019). Coarse scaling laws can relate the observed K2 amplitude to the surface coverage of starspots under assumptions of size, number, and location of spots on a stellar surface (Guo et al. 2018; Rackham et al. 2018). For a K6 spectral type, 0.45% amplitude variations relate (conservatively) to spot-covering fractions of 1%–4% (Rackham et al. 2019). Thus, we adopt a spot contrast typical of a K6 star and a filling factor of 1%–4% (Rackham et al. 2019). Under these assumptions, a planet with a 1% transit depth could expect an H_2O contamination of <15 ppm from unocculted spots. The sub-Neptune GJ 9827 d's much smaller transit depth of <0.1% would therefore yield a negligible TLS water contamination of <1.5 ppm.

We perform a retrieval on our combined transit spectrum in which we fit for TLS parameters rather than atmospheric parameters. We use the 1%–4% spot filling factor as a prior in this TLS retrieval, and the other parameters are the photospheric temperature, the spots' temperature difference, and a scaling factor. Our TLS models simulate unocculted starspots by averaging the stellar spectrum of the star's photoshere with the spectrum of the cooler spots (weighted by the spot coverage) based on Phoenix stellar models (Husser et al. 2013). It then simulates the transit of an airless planet to obtain the stellar-contaminated transit spectrum. When using the photometry-derived prior, we find that the TLS fitting is

restricted to flat models, which indicate that stellar contamination is not expected for that system (Figure 4).

Repeating the same TLS retrieval with nonrestrictive uniform priors on all parameters further demonstrates that the signal cannot be caused by the star. We run the same TLS retrieval as described above but without using the 1%–4% spot filling factor prior to see under what stellar conditions the signal can be explained by the star. We find that, in order for the TLS to reproduce the signal in our spectrum, not only do the spot parameters need to be unrealistically large (73% spot coverage and <-794 K spot temperature difference), but the model needs to adopt a strong positive ramp toward short wavelengths (as in Moran et al. 2023), which becomes inconsistent with the K2 transit depth measurement. We thus conclude that stellar contamination cannot explain the feature in the transmission spectrum of GJ 9827 d and that the water detection comes from the planet's atmosphere.

6. Discussion and Conclusions

The HST/WFC3 transmission spectrum of GJ 9827 d presented in this work provides a precious target in the population of sub-Neptune exoplanets for which we have precise transmission spectra and highlights GJ 9827 d as the smallest exoplanet with an unambiguous atmospheric molecular detection to date. Compared to the other characterized sub-Neptunes, our detection of an $\sim$1 H/He scale height water feature (Figure 6) makes it stronger than for similarly hot sub-Neptunes, although it remains broadly consistent with the previously observed trend, where hotter sub-Neptunes display stronger H_2O amplitudes (Crossfield & Kreidberg 2017). Our analysis of the 10 observations of GJ 9827 d's transits also revealed some variability in this planet's orbit, which is to be considered for further monitoring of the system with state-of-the-art facilities such as JWST. Finally, our detection of a water feature in GJ 9827 d's transit spectrum provides the first detection of water in the atmosphere of a potential water world, which, when combined with GJ 9827 d's large mass-loss rate, provides a first line of evidence for this sub-Neptune hosting a water steam–dominated atmosphere.

6.1. Variability in the Transits of GJ 9827 d

The analysis of the 10 transits of GJ 9827 d with HST revealed a significant variability in the transit timings observed from one visit to the other (Figure 2). While this variation is not surprising for a near-resonant system and did not impact the features observed in the transit spectrum (as shown by our analysis of the relative spectra; Figure 3), it is still in contrast with the previously observed transit timing variations (TTVs) for this system, which were of the order of $\sim$3 minutes (Niraula et al. 2017). However, the 5–10 minute TTVs observed for planet d in this work are consistent with an independent study of the TTVs of the GJ 9827 system combining all photometric and radial velocity data (J. Livingston et al. 2023, in preparation).

The limited number of in-transit data points in the time series in this program could also explain the range of transit depths observed in our results. As described earlier, each HST orbit displays an exponential ramp in time that is fitted by our systematics model. This ramp has a much stronger effect in the first few integrations than in the last few integrations of each orbit, when it has settled. Thus, HST/WFC3 observations inherently provide better-quality observations toward the end of each orbit. When considering the individual visits in our program, it seems that egress visits yield deeper transit depths than mid-transit or ingress visits (Figures 1 and 3). This could then be explained by the fact that the different visits in our data set have varying in-transit data quality depending on whether the late orbit integrations are in the transit (ingress and mid-transit visits) or the baseline (egress visits). For instance, visit 6, which is an egress observation, displays a deeper transit depth than the other visits. However, the relative shape of the transmission spectrum, which is the quantity of interest for this work, is consistent with the other visits (Figure 3).

Another potential source of the TTV and transit depth variability observed in our program is starspot crossing. The star GJ 9827 has been shown to display quasiperiodic flux ($\sim$0.45%) variations with a period of $\sim$30 days (Prieto-Arranz et al. 2018; Rodriguez et al. 2018; Teske et al. 2018; Rice et al. 2019; Kosiarek et al. 2021). If these stellar variations were caused by stellar spots, then using a fixed orbital solution and a transit model that does not include the effect of spots in our light-curve fits could lead to biases in our retrieved parameters.

Because of the variability discussed above, we decided to fix the orbital solution and limb-darkening coefficients for the light-curve fits in our program (Section 3). In order to ensure that the limb-darkening coefficients and stellar parameters chosen do not affect our atmospheric inference, we repeat our light-curve fits for multiple assumptions on the limb darkening. Using quadratic limb-darkening coefficients, we reproduce the same fitting but using a 3D stellar model (Magic et al. 2015) when computing the coefficients. We further try the light-curve fits by varying the effective stellar temperature to the $+1\sigma$ and -1σ values of that parameter (Kosiarek et al. 2021). In all cases, we find that the limb darkening and choice of stellar parameters only affect the retrieved spectrum with a constant offset throughout the wavelength range, and that the relative spectra all show the water absorption feature and are all consistent within 1σ. This thus shows that our choice for the stellar and limb-darkening parameters does not affect the shape of the transmission spectrum and, subsequently, our atmospheric analysis.

Similarly, given the difficult observational setting, we test the robustness of the spectrum to the systematics models used by trying two alternative light-curve fitting methods. First, we start from the divide-white corrected spectroscopic light curves and jointly fit a relative transmission spectrum. To do so, we jointly fit (across visits) the relative transit depth in each channel, where the broadband average of the individually fitted spectra is subtracted for each visit (since there are sometimes discrepancies between the white light-curve transit depths and the average spectral depths in HST/WFC3 data). Second, we repeat the method presented in Section 3 but using the RECTE systematics model and orbit 1 (and not using the divide-white method; Zhou et al. 2017) for the seven visits that are not affected by transits of planet b in orbits 1 or 2. This gives us seven transmission spectra that we combine with a weighted average. Both of these methods produce relative transmission spectra that are consistent within the uncertainties with the one presented in Table 1. The spectrum obtained from the RECTE models has increased uncertainties, both from the smaller number of visits and from increased fitted scatter in some visits, but is still in agreement with the other two spectra. The spectrum presented in this work is thus robust to the choice of systematics model.

6.2. Water in the Envelope of a Potential Water World

The water detection in the transit spectrum of GJ 9827 d makes it the first water world candidate with an atmospheric water detection consistent with a water-rich envelope. It thus positions itself in the sample of potential water worlds with other small sub-Neptunes and super-Earths such as Kepler-138 d (Piaulet et al. 2023), L98-59 d (Kostov et al. 2019), TOI-1685 b (Bluhm et al. 2021), GJ 3090 d (Almenara et al. 2022), and TOI-270 d (Günther et al. 2019, Mikal-Evans et al. 2023). In contrast, a water feature was also detected in the transit spectrum of TOI-270 d (Mikal-Evans et al. 2023), but the analysis revealed that the H-rich atmosphere scenario was favored for this sub-Neptune, showing that the line can be fine between a mini-Neptune and a water world.

With its small mass of 3.42 $M_\oplus$ (Kosiarek et al. 2021) and its proximity to its host star (6.2 day orbit), the estimated mass-loss rate of GJ 9827 d is $>0.5\,M_\oplus\,\mathrm{Gyr}^{-1}$ (Krishnamurthy et al. 2023). With an estimated age of around 6 Gyr (Kosiarek et al. 2021), GJ 9827 d is unlikely to retain an extended H_2/He envelope today. Furthermore, monitoring of GJ 9827 d's spectrum in the search of Hα and He I signatures with Keck/NIRSPEC (Kasper et al. 2020), CARMENES (Carleo et al. 2021), and IRD (Krishnamurthy et al. 2023) resulted in no evidence of an extended H_2/He atmosphere around the planet. Hence, the H-rich scenario with a smaller water abundance would provide a somewhat contradictory statement to the previous studies that observed GJ 9827 d from the ground. However, the water-rich scenario can explain both the observed HST transit spectrum and the nondetection of Hα/He I lines from ground-based studies. The water-dominated envelope is thus the compositional scenario that explains all of the data at hand on this system in the most natural way.

In this water-rich scenario, GJ 9827 d would thus represent a larger, hotter, close-in version of the icy moons of the giant planets in the solar system. Indeed, water is believed to be the dominant volatile of the icy moons of the solar system (Schubert et al. 2004). The sub-Neptune GJ 9827 d could then have formed outside of the water-ice line, where water ice is available in large amounts as a planetary building block (Mousis et al. 2019; Venturini et al. 2020). It could then have migrated toward its current stable near-resonant orbit, during which the increasingly important stellar irradiation would have driven an important H_2/He loss, and it would be observed today with a high mean molecular weight water vapor atmosphere due to its warm temperature (Adams et al. 2008; Pierrehumbert 2023) and H_2/He depletion.

While our transmission spectrum cannot unambiguously distinguish between the H-rich and H-depleted scenarios, we have provided the first water detection in the envelope of a water world candidate, making it a key target for further monitoring with JWST. Transmission spectroscopy of GJ 9827 d with NIRISS/SOSS and NIRSpec/G395H would provide the high-precision continuous viewing of the full transit of the planet that is needed to explain the variability observed with HST, as well as a more precise transmission spectrum that could probe not only the water absorption bands but also the presence of carbon-bearing species like CO and CO_2 above 4 μm. A JWST transmission spectrum of GJ 9827 d would thus lift the degeneracy observed in our study (Figure 4) and potentially confirm the water world nature of this sub-Neptune, simultaneously yielding the first direct detection of a water vapor–dominated envelope.

Acknowledgments

All of the data presented in this paper were obtained from the Mikulski Archive for Space Telescopes (MAST) at the Space Telescope Science Institute. The specific observations analyzed can be accessed via 10.17909/dvqh-2r48.

We wish to thank the reviewer for the insightful comments that enhanced the quality of our manuscript. P.-A.R. further thanks L. Bazinet, L.-P. Coulombe, and S. Pelletier for their help, comments, and ideas throughout the multiple iterations of this work.

This work is based on observations with the NASA/ESA HST, obtained at the Space Telescope Science Institute (STScI) operated by AURA, Inc. P.-A.R., B.B., and C.P. acknowledge financial support from the Natural Sciences and Engineering Research Council (NSERC) of Canada. P.-A.R. and C.P. further acknowledge support from the University of Montreal and the Trottier Institute for Exoplanets (iREx). B.B. also acknowledges financial support from the Fond de Recherche Québécois-Nature et Technologie (FRQNT; Québec).

ORCID iDs

Pierre-Alexis Roy https://orcid.org/0000-0001-6809-3520
Björn Benneke https://orcid.org/0000-0001-5578-1498
Caroline Piaulet https://orcid.org/0000-0002-2875-917X
Michael A. Gully-Santiago https://orcid.org/0000-0002-4020-3457
Caroline V. Morley https://orcid.org/0000-0002-4404-0456
Laura Kreidberg https://orcid.org/0000-0003-0514-1147
Thomas Mikal-Evans https://orcid.org/0000-0001-5442-1300
Jonathan Brande https://orcid.org/0000-0002-2072-6541
Simon Delisle https://orcid.org/0000-0002-4771-0312
Thomas P. Greene https://orcid.org/0000-0002-8963-8056
Kevin K. Hardegree-Ullman https://orcid.org/0000-0003-3702-0382
Travis Barman https://orcid.org/0000-0002-7129-3002
Jessie L. Christiansen https://orcid.org/0000-0002-8035-4778
Diana Dragomir https://orcid.org/0000-0003-2313-467X
Jonathan J. Fortney https://orcid.org/0000-0002-9843-4354
Andrew W. Howard https://orcid.org/0000-0001-8638-0320
Molly R. Kosiarek https://orcid.org/0000-0002-6115-4359
Joshua D. Lothringer https://orcid.org/0000-0003-3667-8633

References

Acuña, L., Lopez, T. A., Morel, T., et al. 2022, A&A, 660, A102
Adams, E. R., Seager, S., & Elkins-Tanton, L. 2008, ApJ, 673, 1160
Aguichine, A., Mousis, O., Deleuil, M., & Marcq, E. 2021, ApJ, 914, 84
Almenara, J. M., Bonfils, X., Otegi, J. F., et al. 2022, A&A, 665, A91
Benneke, B. 2015, arXiv:1504.07655
Benneke, B., Knutson, H. A., Lothringer, J., et al. 2019a, NatAs, 3, 813
Benneke, B., & Seager, S. 2012, ApJ, 753, 100
Benneke, B., & Seager, S. 2013, ApJ, 778, 153
Benneke, B., Werner, M., Petigura, E., et al. 2017, ApJ, 834, 187
Benneke, B., Wong, I., Piaulet, C., et al. 2019b, ApJL, 887, L14
Bézard, B., Charnay, B., & Blain, D. 2022, NatAs, 6, 537
Bluhm, P., Pallé, E., Molaverdikhani, K., et al. 2021, A&A, 650, A78
Carleo, I., Youngblood, A., Redfield, S., et al. 2021, AJ, 161, 136
Crossfield, I. J. M., & Kreidberg, L. 2017, AJ, 154, 261
Foreman-Mackey, D., Hogg, D. W., Lang, D., & Goodman, J. 2013, PASP, 125, 306
Fulton, B. J., & Petigura, E. A. 2018, AJ, 156, 264

Fulton, B. J., Petigura, E. A., Howard, A. W., et al. 2017, AJ, 154, 109
Grant, D., & Wakeford, H. R. 2022, Exo-TiC/ExoTiC-LD: ExoTiC-LD v3.0.0, Zenodo, doi:10.5281/zenodo.7437681
Günther, M. N., Pozuelos, F. J., Dittmann, J. A., et al. 2019, NatAs, 3, 1099
Guo, Z., Gully-Santiago, M., & Herczeg, G. J. 2018, ApJ, 868, 143
Hardegree-Ullman, K. K., Zink, J. K., Christiansen, J. L., et al. 2020, ApJS, 247, 28
Husser, T.-O., Wende-von Berg, S., Dreizler, S., et al. 2013, A&A, 553, A6
Kasper, D., Bean, J. L., Oklopčić, A., et al. 2020, AJ, 160, 258
Kempton, E. M.-R., Zhang, M., Bean, J. L., et al. 2023, Natur, 620, 67
Knutson, H. A., Benneke, B., Deming, D., & Homeier, D. 2014, Natur, 505, 66
Kosiarek, M. R., Berardo, D. A., Crossfield, I. J. M., et al. 2021, AJ, 161, 47
Kostov, V. B., Schlieder, J. E., Barclay, T., et al. 2019, AJ, 158, 32
Kreidberg, L. 2015, PASP, 127, 1161
Kreidberg, L., Bean, J. L., Désert, J.-M., et al. 2014, Natur, 505, 69
Kreidberg, L., Mollière, P., Crossfield, I. J. M., et al. 2022, AJ, 164, 124
Krishnamurthy, V., Hirano, T., Gaidos, E., et al. 2023, MNRAS, 521, 1210
Kurucz, R.-L. 1993, Kurucz CD-Rom (Cambridge, MA: Smithsonian Astrophysical Observatory), 13
Luque, R., & Pallé, E. 2022, Sci, 377, 1211
Magic, Z., Chiavassa, A., Collet, R., & Asplund, M. 2015, A&A, 573, A90
Mikal-Evans, T., Crossfield, I. J. M., Benneke, B., et al. 2020, AJ, 161, 18
Mikal-Evans, T., Madhusudhan, N., Dittmann, J., et al. 2023, AJ, 165, 84
Moran, S. E., Stevenson, K. B., Sing, D. K., et al. 2023, ApJL, 948, L11
Mousis, O., Ronnet, T., & Lunine, J. I. 2019, ApJ, 875, 9
Niraula, P., Redfield, S., Dai, F., et al. 2017, AJ, 154, 266
Owen, J. E. 2019, AREPS, 47, 67
Owen, J. E., & Lai, D. 2018, MNRAS, 479, 5012
Pelletier, S., Benneke, B., Darveau-Bernier, A., et al. 2021, AJ, 162, 73
Piaulet, C., Benneke, B., Almenara, J. M., et al. 2023, NatAs, 7, 206
Pierrehumbert, R. T. 2023, ApJ, 944, 20
Prieto-Arranz, J., Palle, E., Gandolfi, D., et al. 2018, A&A, 618, A116
Rackham, B. V., Apai, D., & Giampapa, M. S. 2018, ApJ, 853, 122
Rackham, B. V., Apai, D., & Giampapa, M. S. 2019, AJ, 157, 96
Rice, K., Malavolta, L., Mayo, A., et al. 2019, MNRAS, 484, 3731
Rodriguez, J. E., Vanderburg, A., Eastman, J. D., et al. 2018, AJ, 155, 72
Rogers, J. G., Schlichting, H. E., & Owen, J. E. 2023, ApJL, 947, L19
Rogers, L. A., & Seager, S. 2010, ApJ, 716, 1208
Roy, P.-A., Benneke, B., Piaulet, C., et al. 2022, ApJ, 941, 89
Schubert, G., Anderson, J. D., Spohn, T., & McKinnon, W. B. 2004, Jupiter. The planet, satellites and magnetosphere., Vol. 1 (Cambridge: Cambridge Univ. Press), 281
Skilling, J. 2004, in AIP Conf.Proc. 735, Bayesian Inference and Maximum Entropy Methods in Science and Engineering: 24th International Workshop on Bayesian Inference and Maximum Entropy Methods in Science and Engineering, ed. R. Rainer, R. Preuss, & U. von Toussaint (Melville, NY: AIP), 395
Skilling, J. 2006, BayAn, 1, 833
Stevenson, K. B., Bean, J. L., Seifahrt, A., et al. 2014, AJ, 147, 161
Teske, J. K., Wang, S., Wolfgang, A., et al. 2018, AJ, 155, 148
Vanderburg, A., & Johnson, J. A. 2014, PASP, 126, 948
Van-Eylen, V., Agentoft, C., Lundkvist, M. S., et al. 2018, MNRAS, 479, 4786
Venturini, J., Guilera, O. M., Haldemann, J., Ronco, M. P., & Mordasini, C. 2020, A&A, 643, L1
Zhou, Y., Apai, D., Lew, B. W. P., & Schneider, G. 2017, AJ, 153, 243